Numerical modelling of a slope stability test by means of porous media mechanics

Lorenzo Sanavia

Dipartimento di Costruzioni e Trasporti
Università degli Studi di Padova
35131 Padova, Italia
e-mail: lorenzo.sanavia@unipd.it

Dedicated to Professor Bernhard A. Schrefler on the occasion of his 65th birthday

April 18, 2008

Paper Engineering Computations n. 1258 revised

Keywords: Poromechanics, Multiphase porous material, Thermo-Hydro-Mechanical modelling, Initiation of landslides, Finite element modelling, Coupled problems

Abstract. In this work a finite element analysis of a slope instability due to capillary and water pressure variation is presented. To this aim, a non-isothermal elasto-plastic multiphase material model for soils is used. Soils are described as a three-phase deforming porous continuum where heat, water and gas flow are taken into account. In particular, the gas phase is modelled as an ideal gas composed of dry air and water vapor. Phase changes of water, heat transfer through conduction and convection and latent heat transfer are considered. The independent variables are the solid displacements, the capillary and the gas pressure and the temperature. The effective stress state is limited by Drucker-Prager yield surface for simplicity. Small strains and quasi-static loading conditions are assumed. Numerical simulation of a partially saturated slope stability experiment is presented assuming plane strain condition during the computations.

1 Introduction

In recent years, increasing interest in thermo-hydro-mechanical (THM) analysis of saturated and partially saturated materials has been observed, because of its wide spectrum of engineering applications. Typical examples belong to environmental geomechanics, where some challenging problems are of interest for the research community.

Landslides and slopes failure are one of these important problems, because they may cause loss of life, human injury and economic devastation. There

is a wide variety of types of landslides, depending on the triggering mechanisms, the kind of propagation and the materials involved, (e.g. Dikau et al., 1996; Bolton et al., 2003). Landslides are caused by changes of effective stress induced by external forces (earthquake, human action) and/or variation of the pore pressures due, e.g., to rainfall, variation of the material properties (e.g. due to degradation by weathering and chemical attack) and changes in geometry (due, e.g., to erosion or or human action like excavation). In some cases, the failure mechanism consists of a clearly defined localized zone, while in other cases a diffuse type develops. From an engineering point of view, the prediction of the initiation and propagation of such events are important and expected also from the social community.

Several authors are working worldwide on the numerical simulation of slope instability. Among them, the modelling of diffuse failure mechanism and the propagation of fast landslides are presented in Fernandez Merodo et al. (2004), Pastor et al. (2004a) and Pastor et al. (2004b), Pastor et al. (2004c), respectively. An example dealing with an excavation problem is studied by Ehlers et al. (2004) with a triphasic elasto-plastic isothermal model; a three-phasic elastic isothermal model was used in Klubertanz (1999) and Klubertanz et al. (2003) to simulate a small-scale slope stability test. An application of a water saturated model was done by Tacher et al. (2005) to determine the pore pressure fields in La Frasse landslide mass (CH) during a crisis.

Often, the approach for landslide simulation in engineering practice is uncoupled in the sense that a seepage analysis is performed first, followed by a limit analysis (e.g. Cascini et al. (2005), which analyzes the onset of landslides in pyroclastic soils).

In this work, a fully coupled, non-isothermal and transient analysis is adopted and an application to the initiation of landslides due to capillary/water pressure variation is considered. To this end, a 2-D partially saturated slope stability experiment (Klubertanz, 1999; Klubertanz et al., 2003), is simulated by using the geometrically linear finite element code Comes-Geo (Lewis and Schrefler, 1998) for non-isothermal elasto-plastic multiphase solid porous materials as developed by Sanavia et al. (2006).

In the following, we summarize the mathematical and finite element model in Section 2. The multiphase material is described as a deforming porous continuum where heat, water and gas flow are taken into account (Lewis and Schrefler, 1998; Gawin et al., 1995; Schrefler, 2002). Small strains and quasi-static loading conditions are assumed. The elasto-plastic behaviour of the solid skeleton is assumed homogeneous and isotropic; the effective stress state is limited by a temperature independent Drucker-Prager yield surface for simplicity, with linear isotropic hardening and non associated plastic flow, as summarized in Section 2.2. The model equations are discretized in space and time within the finite element method in Section 2.3. In particular, a Galerkin procedure is used for the discretization in space and the General-

ized Trapezoidal Method is used for the time integration. Finally, the finite element results of the 2-D partially saturated slope stability experiment described in Section 3 are presented in Section 4.

This example has been simulated to emphasize the importance of the multiphase modelling for the simulation of the hydro-thermo-mechanical behavior of partially saturated slopes at the onset of failure. It can be considered as a step in the development of a suitable numerical model for the simulation of non-isothermal geo-environmental engineering problems.

For the description of the propagation phase, a different approach has to be followed since it is characterized by very large displacements and a change in the material structure, as e.g. the fluidization (Pastor et al., 2004c).

2 Mathematical and Finite Element Model

The mathematical model necessary to simulate the thermo-hydro-mechanical transient behaviour of fully and partially saturated porous media is developed in Sanavia et al. (2006) following the works by Lewis and Schrefler (1998) and Schrefler (2002) and using averaging theories by Hassanizadeh and Gray (1979a,b, 1980). The model is briefly summarized in the present section for sake of completeness.

The partially saturated porous medium is treated as multiphase system composed of a solid skeleton (s) with open pores filled with water (w) and gas (g). The latter is assumed to behave as an ideal mixture of two species: dry air (non-condensable gas, ga) and water vapour (condensable one, gw).

At the macroscopic level the porous media material is modelled by a substitute continuum of volume B_t with boundary ∂B_t that fills the entire domain simultaneously, instead of the real fluids and the solid which fill only a part of it. In this substitute continuum each constituent π has a reduced density which is obtained through the volume fraction $\eta^\pi(\mathbf{x},t) = dv^\pi(\mathbf{x},t)/dv(\mathbf{x},t)$ where $\mathbf{x}$ is the vector of the spatial coordinates, t is the current time and $\pi = s, w, g$. In the model, heat conduction, vapour diffusion, heat convection, water flow due to pressure gradients or capillary effects and water phase change (evaporation and condensation) inside the pores are taken into account. The solid skeleton is deformable; the solid and water constituents are assumed incompressible at microscopic level and non-polar, while gas is considered compressible. The fluids, the solid and the thermal fields are coupled. All fluids are in contact with the solid phase. The constituents are assumed to be isotropic, homogeneous, immiscible except for dry air and vapour, and chemically non reacting. Local thermal equilibrium between solid matrix, gas and liquid phases is assumed. The model is developed in the geometrically linear framework by considering quasi-static loading conditions. The state of the medium is described by capillary pressure p^c, gas pressure p^g, absolute temperature T and displacements of the solid matrix $\mathbf{u}$.

In the partially saturated zones water is separated from its vapour by a concave meniscus (capillary water). Due to the curvature of this meniscus the sorption equilibrium equation (e.g. Gray and Hassanizadeh, 1991) gives the relationship between the capillary pressure $p^c(\mathbf{x},t)$, the gas pressure $p^g(\mathbf{x},t)$ and water pressure $p^w(\mathbf{x},t)$ (Gray and Hassanizadeh, 1991)

$$p^c = p^g - p^w \tag{1}$$

Pore pressure is defined as compressive positive for the fluids, while stress is defined as tension positive for the solid phase. For a detailed discussion about the chosen primary variables see Sanavia et al. (2006). The balance equations of the implemented model are now summarized.

2.1 Macroscopic Balance Equations

The linear momentum balance equation of the mixture in terms of modified Cauchy effective stress $\boldsymbol{\sigma}'(\mathbf{x},t)$, also called generalized Bishop stress tensor (Nuth and Laloui, 2008), assumes the form

$$div(\boldsymbol{\sigma}' - [p^g - S_w p^c]\mathbf{1}) + \rho\mathbf{g} = \mathbf{0} \tag{2}$$

where $\rho(\mathbf{x},t)$ is the density of the mixture. $\rho = [1-n]\rho^s + nS_w\rho^w + nS_g\rho^g$, with $n(\mathbf{x},t)$ the porosity, $S_w(\mathbf{x},t)$, and $S_g(\mathbf{x},t)$ the water and gas degree of saturation, respectively and $\mathbf{1}$ is the second order identity tensor. This form using saturation as weighting functions for the partial pressures was first introduced by Schrefler (1984) using volume averaging (see also Lewis and Schrefler, 1987; Schrefler et al., 1990) and is thermodynamically consistent (Gray and Hassanizadeh, 1991; Gray and Schrefler, 2001; Borja, 2004).

The mass conservation equation for the water and the vapour is

$$\begin{aligned}
&n[\rho^w - \rho^{gw}]\frac{\partial S_w}{\partial t} + [\rho^w S_w - \rho^{gw}[1-S_w]]\,\mathrm{div}\left(\frac{\partial \mathbf{u}}{\partial t}\right) \\
&+n[1-S_w]\frac{\partial \rho^{gw}}{\partial t} - \mathrm{div}\left(\rho^g \frac{M_a M_w}{M_g^2}\mathbf{D}_g^{gw}\mathrm{grad}\left(\frac{p^{gw}}{p^g}\right)\right) \\
&+\mathrm{div}\left(\rho^w \frac{\mathbf{k}\,k^{rw}}{\mu^w}[-\mathrm{grad}p^g + \mathrm{grad}p^c + \rho^w\mathbf{g}]\right) \\
&+\mathrm{div}\left(\rho^{gw}\frac{\mathbf{k}\,k^{rg}}{\mu^g}[-\mathrm{grad}p^g + \rho^g\mathbf{g}]\right) - \beta_{swg}\frac{\partial T}{\partial t} = 0
\end{aligned} \tag{3}$$

where, in particular, $\mathbf{k}(\mathbf{x},\,t)$ is the intrinsic permeability tensor, $k^{r\pi}(\mathbf{x},\,t)$ the fluid relative permeability ($\pi = w, g$), $\mu^\pi(\mathbf{x},\,t)$ the fluid viscosity and $\beta_{swg} = \beta_s[1-n][S_g\rho^{gw} + S_w\rho^w] + n\beta_w S_w\rho^w$. $\beta_s(\mathbf{x},\,t)$ and $\beta_w(\mathbf{x},\,t)$ are the solid and water cubic thermal expansion coefficient, respectively. The inflow and outflow fluxes have been described using the Fick law for the diffusion of the

vapour in the gas phase and by the Darcy law for the water and gas flows. $\mathbf{D}_g^{gw}$ is the effective diffusivity tensor of water vapour in dry air, and M_a, M_w and $M_g(\mathbf{x}, t)$ the molar mass of dry air, water and gas mixture, respectively.

Similarly, the mass balance equation for the dry air is

$$\begin{aligned} &-n\rho^{ga}\frac{\partial S_w}{\partial t} + nS_g\frac{\partial \rho^{ga}}{\partial t} + [1-S_w]\rho^{ga}\mathrm{div}\left(\frac{\partial \mathbf{u}}{\partial t}\right) \\ &+\mathrm{div}\left(\rho^{ga}\frac{\mathbf{k}\,k^{rg}}{\mu^g}[-\mathrm{grad}(p^g)+\rho^g\mathbf{g}]\right) \\ &-\mathrm{div}\left(\rho^g\frac{M_aM_w}{M_g^2}\mathbf{D}_g^{ga}\mathrm{grad}\left(\frac{p^{ga}}{p^g}\right)\right) - \beta_s\rho^{ga}[1-n][1-S_w]\frac{\partial T}{\partial t} = 0 \end{aligned} \tag{4}$$

The quantities $S_w(\mathbf{x}, t)$, $S_g(\mathbf{x}, t)$, $k^{rw}(\mathbf{x}, t)$ and $k^{rg}(\mathbf{x}, t)$ are defined at the constitutive level, as described in Section 2.2.

The energy balance equation of the mixture is

$$\begin{aligned} &(\rho C_p)_{eff}\frac{\partial T}{\partial t} + \rho^w C_p^w\left[\frac{\mathbf{k}\,k^{rw}}{\mu^w}[-\mathrm{grad}(p^g)+\mathrm{grad}(p^c)+\rho^w\mathbf{g}]\right]\cdot\mathrm{grad}(T) \\ &+\rho^g C_p^g\left[\frac{\mathbf{k}\,k^{rg}}{\mu^g}[-\mathrm{grad}(p^g)+\rho^g\mathbf{g}]\right]\cdot\mathrm{grad}(T) - \mathrm{div}(\chi_{eff}\mathrm{grad}(T)) = \\ &-\dot{m}_{vap}\Delta H_{vap} \end{aligned} \tag{5}$$

where, in particular, $\dot{m}_{vap}\Delta H_{vap}$ considers the contribution of the evaporation and condensation. $(\rho C_p)_{eff}(\mathbf{x}, t)$ is the effective thermal capacity of porous medium, $C_p^w(\mathbf{x}, t)$ and $C_p^g(\mathbf{x}, t)$ the specific heat of water and gas mixture, respectively and $\chi_{eff}(\mathbf{x}, t)$ the effective thermal conductivity of the porous medium. This balance equation takes into account the heat transfer through conduction and convection as well as latent heat transfer (see Lewis and Schrefler, 1998) and neglects the terms related to the mechanical work induced by density variations due to temperature changes of the phases and induced by volume fraction changes.

2.2 Constitutive Equations, Initial and Boundary Conditions

For a gaseous mixture of dry air and water vapour, the ideal gas law is introduced because the moist air is assumed to be a perfect mixture of two ideal gases. The equation of state of perfect gas (the Clapeyron equation) and Dalton's law are applied to dry air (ga), water vapour (gw) and moist air (g). In the partially saturated zones, the water vapour pressure $p^{gw}(\mathbf{x}, t)$ is obtained from the Kelvin-Laplace equation

$$p^{gw} = p^{gws}(T)\,\exp\left(-\frac{p^c\,M_w}{\rho^w\,R\,T}\right) \tag{6}$$

where the water vapour saturation pressure $p^{gws}(\mathbf{x},\, t)$, depending only upon the temperature $T(\mathbf{x},\, t)$, can be calculated from the Clausius-Clapeyron equation or from an empirical correlation. R is the gas constant. The saturation $S_\pi(\mathbf{x},\, t)$ and the relative permeability $k^{r\pi}(\mathbf{x},\, t)$ are experimentally determined function of the capillary pressure p^c and the temperature T

$$S_\pi = S_\pi(p^c,\, T)\,, \qquad k^{r\pi} = k^{r\pi}(p^c,\, T)\,, \qquad \pi = w, g \tag{7}$$

The elasto-plastic behaviour of the solid skeleton is assumed to be described within the classical rate-independent elasto-plasticity theory for geometrically linear problems. The yield function $F(p', \mathbf{s}', \xi)$ restricting the modified effective stress state $\boldsymbol{\sigma}'(\mathbf{x}, t)$ is developed in the form of Drucker-Prager for simplicity (Sanavia et al., 2006),

$$F(p', \mathbf{s}', \xi) = 3\alpha_F p' + \|\mathbf{s}'\| - \beta_F \sqrt{\frac{2}{3}}[c_0 + h\xi] \tag{8}$$

to take into account the dilatant/contractant behaviour of dense or loose sands, respectively. In eq. (8), $p' = \frac{1}{3}[\boldsymbol{\sigma}' : \mathbf{1}]$ is the mean effective Cauchy pressure, $\|\mathbf{s}'\|$ is the L_2 norm of the deviator effective Cauchy stress tensor $\boldsymbol{\sigma}'$, c_0 is the apparent cohesion, α_F and β_F are two material parameters related to the friction angle ϕ of the soil

$$\alpha_F = 2\frac{\sqrt{\frac{2}{3}}\sin\phi}{3 - \sin\phi} \qquad\qquad \beta_F = \frac{6\cos\phi}{3 - \sin\phi} \tag{9}$$

and h and ξ the hardening/softening modulus and the equivalent plastic strain variable, respectively.

Remarks: in the present contribution, the effect of the capillary pressure p^c and of the temperature T on the evolution of the yield surface is not taken into account. The interested reader can refers, e.g., to Alonso et al. (1990), Bolzon et al. (1996) and Borja (2004) for capillary dependent constitutive relationships and to Zhang et al. (2000) for the numerical implementation of constitutive law proposed by Bolzon et al. (1996). A model for non-isothermal unsaturated soils has recently been proposed by Bertand and Laloui (2008).

For the model closure the initial and boundary conditions are needed. The initial conditions specify the full fields of primary state variables at time $t = t_0$, in the whole analyzed domain B and on its boundary ∂B, ($\partial B = \partial B_\pi \cup \partial B^q_\pi$, π=$g,\ c,\ T,\ u$):

$$p^g = p^g_0,\ p^c = p^c_0,\ T = T_0,\ \mathbf{u} = \mathbf{u}_0, \quad \text{on} \quad B \cup \partial B, \tag{10}$$

The boundary conditions (BCs) can be of Dirichlet's type on ∂B_π for $t \geq t_0$:

$$\begin{array}{l} p^g = \hat{p}^g \quad \text{on} \quad \partial B_g, \quad p^c = \hat{p}^c \quad \text{on} \quad \partial B_c, \\ T = \hat{T} \quad \text{on} \quad \partial B_T, \quad \mathbf{u} = \hat{\mathbf{u}} \quad \text{on} \quad \partial B_u \end{array} \tag{11}$$

or of Cauchy's type (the mixed BCs) on ∂B_π^q for $t \geq t_0$:

$$\begin{aligned}
&(nS_g\rho^{ga}\mathbf{v}^{gs} + \mathbf{J}_d^{ga}) \cdot \mathbf{n} = q^{ga} \quad \text{on} \quad \partial B_g^q \\
&(nS_w\rho^w\mathbf{v}^{ws} + nS_g\rho^{gw}\mathbf{v}^{gs} + \mathbf{J}_d^{gw}) \cdot \mathbf{n} \\
&= q^{gw} + q^w + \beta_c\,(\rho^{gw} - \rho_\infty^{gw}) \quad \text{on} \quad \partial B_c^q \\
&(nS_w\rho^w\mathbf{v}^{ws}\Delta H_{vap} - \chi_{eff}\,grad\,T) \cdot \mathbf{n} \\
&= q^T + \alpha_c\,(T - T_\infty) + e\,\sigma_o\left(T^4 - T_\infty^4\right) \quad \text{on} \quad \partial B_T^q \\
&\boldsymbol{\sigma} \cdot \mathbf{n} = \bar{\mathbf{t}} \quad \text{on} \quad \partial B_u^q
\end{aligned} \tag{12}$$

where $\mathbf{n}(\mathbf{x}, t)$ is the unit normal vector, pointing toward the surrounding gas and $q^{ga}(\mathbf{x}, t), q^{gw}(\mathbf{x}, t), q^w(\mathbf{x}, t)$ and $q^T(\mathbf{x}, t)$ are the imposed fluxes of dry air, vapour, liquid water and the imposed heat flux, respectively. $\bar{\mathbf{t}}(\mathbf{x}, t)$ is the imposed traction vector related to the total Cauchy stress tensor $\boldsymbol{\sigma}(\mathbf{x}, t)$. $\rho_\infty^{gw}(\mathbf{x}, t)$ and $T_\infty(\mathbf{x}, t)$ are the mass concentration of water vapour and the temperature in the far field of undisturbed gas phase, $e(\mathbf{x}, t)$ the emissivity of the interface and σ_o the Stefan-Boltzmann constant. $\alpha_c(\mathbf{x}, t)$ and $\beta_c(\mathbf{x}, t)$ are convective heat and mass exchange coefficients, respectively.

2.3 Finite Element Formulation

The finite element model is derived by applying the Galerkin procedure for the spatial integration and the Generalized Trapezoidal Method for the time integration of the weak form of the balance equations of Section 2.1 (see e.g. Lewis and Schrefler, 1998; Zienkiewicz et al., 1999).

In particular, after spatial discretization within the isoparametric formulation, a non-symmetric, non-linear and coupled system of equation is obtained

$$\begin{bmatrix} \mathbf{C}_{gg} & \mathbf{C}_{gc} & \mathbf{C}_{gt} & \mathbf{C}_{gu} \\ \mathbf{0} & \mathbf{C}_{cc} & \mathbf{C}_{ct} & \mathbf{C}_{cu} \\ \mathbf{0} & \mathbf{C}_{tc} & \mathbf{C}_{tt} & \mathbf{C}_{tu} \\ \mathbf{0} & \mathbf{0} & \mathbf{0} & \mathbf{0} \end{bmatrix} \begin{bmatrix} \dot{\bar{\mathbf{p}}}^g \\ \dot{\bar{\mathbf{p}}}^c \\ \dot{\bar{\mathbf{T}}} \\ \dot{\bar{\mathbf{u}}} \end{bmatrix} + \begin{bmatrix} \mathbf{K}_{gg} & \mathbf{K}_{gc} & \mathbf{K}_{gt} & \mathbf{0} \\ \mathbf{K}_{cg} & \mathbf{K}_{cc} & \mathbf{K}_{ct} & \mathbf{0} \\ \mathbf{K}_{tg} & \mathbf{K}_{tc} & \mathbf{K}_{tt} & \mathbf{0} \\ \mathbf{K}_{ug} & \mathbf{K}_{uc} & \mathbf{K}_{ut} & \mathbf{K}_{uu} \end{bmatrix} \begin{bmatrix} \bar{\mathbf{p}}^g \\ \bar{\mathbf{p}}^c \\ \bar{\mathbf{T}} \\ \bar{\mathbf{u}} \end{bmatrix} = \begin{bmatrix} \mathbf{f}_g \\ \mathbf{f}_c \\ \mathbf{f}_t \\ \mathbf{f}_u \end{bmatrix} \tag{13}$$

where the solid displacements $\mathbf{u}(\mathbf{x}, t)$, the capillary and the gas pressure $p^c(\mathbf{x}, t)$ and $p^g(\mathbf{x}, t)$ and the temperature $T(\mathbf{x}, t)$ are expressed in the whole domain by global shape function matrices $\mathbf{N}_u(\mathbf{x})$, $\mathbf{N}_c(\mathbf{x})$, $\mathbf{N}_g(\mathbf{x})$, $\mathbf{N}_T(\mathbf{x})$ and the nodal value vectors $\bar{\mathbf{u}}(t)$, $\bar{\mathbf{p}}^c(t)$, $\bar{\mathbf{p}}^g(t)$ and $\bar{\mathbf{T}}(t)$

$$\mathbf{u} = \mathbf{N}_u\bar{\mathbf{u}}\,, \qquad \mathbf{p}^c = \mathbf{N}_c\bar{\mathbf{p}}^c\,, \qquad \mathbf{p}^g = \mathbf{N}_g\bar{\mathbf{p}}^g\,, \qquad T = \mathbf{N}_T\bar{\mathbf{T}} \tag{14}$$

In eq. (13), the symbol $(\dot{\bullet})$ means the time derivative. In the example section, implicit one-step time integration has been performed.

After time integration the non-linear system of equation is linearized consistently with the integrated constitutive equations, thus obtaining the equations system that can be solved numerically. Details concerning the matrices

and the residuum vectors of the linearized equations system can be found in Sanavia et al. (2006). Owing to the strong coupling between the mechanical, thermal and the pore fluids problems, a monolithic solution of the linearized system is preferred using a Newton scheme.

The return mapping and the consistent tangent operator are derived by Sanavia et al. (2006) for isotropic linear hardening/softening and volumetric-deviatoric non-associative plasticity, solving the singular behaviour of the Drucker-Prager yield surface in the zone of the apex using the concept of multisurface plasticity (Sanavia et al., 2002).

3 Experimental test

A 2-D laboratory test was carried out by G. Klubertanz during his PhD thesis at the Soil Mechanics Laboratory of the Swiss Federal Institute of Technology (LMS-EPFL) in Lausanne (Klubertanz, 1999; Klubertanz et al., 2003).

The experiment reproduces a stability problem of a small-scale slope of 1 m hight, 1.5 m in length and 0.25 m wide (Figure 1) due to variations in water pressure boundary condition. To this end, a constant water table was first imposed at the left- and right-hand sides of the slope below the upper surface (at 0.2 and 0.15 m, respectively). Then, a constant water pressure load of 1.6 kPa was applied at the left third of the bottom surface. Water pressure and solid displacements where measured (Klubertanz, 1999; Klubertanz et al., 2003). A local rupture of the lower part of the slope was observed after about $t = 80$ s since the application of the water load at the base of the experimental set-up. The slope continued to fail by backward erosion for further 10 s and outflow appeared at the lower part soon afterwards.

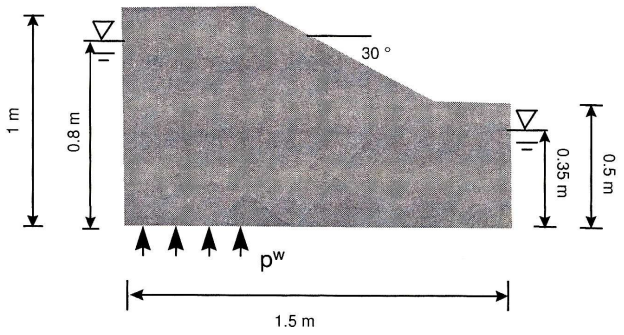

Fig. 1. Description of the geometry, boundary and loading conditions

4 Numerical Results

A finite element analysis of the Klubertanz experimental test has been performed with the non-isothermal elasto-plastic multiphase model presented in the previous sections, with the aim to analyze the hydro-mechanical conditions for the initiation of the slope failure observed at the toe of the slope.

The material parameters used in the computation are listed in Table 1. Most of them have been chosen from the laboratory tests performed on the material (fine silty sand) used for the experiment (see Klubertanz, 1999, for the geotechnical properties). The solid skeleton is assumed to obey the Drucker-Prager constitutive model in isothermal condition, with isotropic linear softening behaviour and non-associated plastic flow. Two cases have been simulated, assuming a dilatant angle of 0^0 and 5^0, respectively (a positive value is more realistic for the material used for the experiment; this choice permits to underline the capabilities of the multiphase modelling, as we will see by analyzing the numerical results). The value of cohesion measured in saturated conditions was about 0 kPa; for numerical purposes, it has been selected to 420 Pa in order to get the failure of the slope at about 90 s with a dilatancy angle of 0^0. The constitutive relationship for the water degree of saturation $S_w(p^c)$ is that of Seker, with the parameters $\Psi_0 = 1.89$ and $\Psi_1 = 0.05$ to fit the experimental retention curve measured by laboratory tests (Klubertanz, 1999). For the water and gas relative permeability, $k^{rw}(S_w)$ and $k^{rg}(S_w)$, the relationships of Safai and Pinder and Brooks and Corey in isothermal condition have been selected, respectively. These relationships have been used because of the lack of experimental results. Plane strain condition has been assumed in the computation.

Table 1. Material parameters used in the computation

solid density	ρ_s	2650	kg/m^3
water density	ρ_w	1000	kg/m^3
Young modulus	E	0.43E+06	Pa
Poisson ratio	ν	0.46	
apparent cohesion	c_0	420	Pa
linear softening modulus	h	-4.30E+04	Pa
angle of internal friction	ϕ	34^0	
angle of dilatancy	φ	0^0 or 5^0	
porosity	n	0.415	
water conductivity in saturated conditions	k_w	8.00E-6	m/s
First $S_w - p^c$ parameter	Ψ_0	1.89	
Second $S_w - p^c$ parameter	Ψ_1	0.05	

We have simulated the experimental test by carrying out three successive runs (the spatial discretization adopted is depicted in Figure 2). With the

first one, a uniform capillary pressure p^c of 9.0 kPa (which correspond to a water saturation S_w of 0.32), a uniform ambient temperature and atmospheric pressure were applied to simulate the almost dry material packed within the experimental box before the application of the constant water tables at the lateral surfaces of the slope. Horizontal displacements of the lateral surfaces and vertical displacements of the lower surface are constrained. The mechanical equilibrium with these thermo-hydro conditions was computed consequently by the model, assuming for the solid skeleton a linear elastic, isotropic and homogeneous constitutive law. The stress state and the state variables computed by this THM analysis form the initial conditions for the successive run.

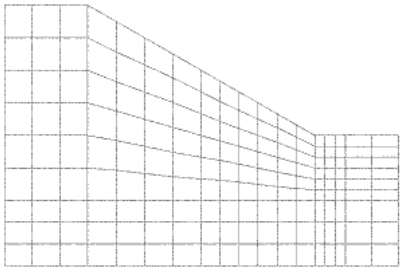

Fig. 2. Finite element mesh used for the computation

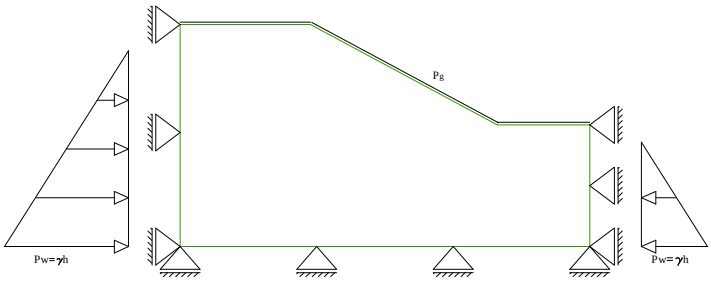

Fig. 3. Boundary conditions of the second run

Then, with the second run, the hydrostatic water load on the lateral surfaces was applied, as depicted in Figure 3. The upper surface is at atmospheric pressure, while the lateral and the lower surfaces are impervious to any fluid flow. The computation was performed until the steady-state condition was reached in the domain (Figure 4, where a uniform water flux distribution can be observed) and the free surface was determined (Figure 5). This free surface is below the upper surface of the slope (Figure 5) and two small partially

saturated zones are obtained, as indicated in Figure 6. The volumetric strain ϵ_v, the mean effective pressure p' and the shear stress τ'_{xy} are depicted in Figure 7, Figure 8 and Figure 9, respectively (again, a linear elastic, isotropic and homogeneous solid material has been assumed). It can be observed that all the solid skeleton is compressed and the lower part of the slope results to be the favorite zone for the initiation of failure because of the lower mean pressure and the higher shear stress. Also the displacements contour reveals that the deformation is higher in the lower part of the slope (Figure 10).

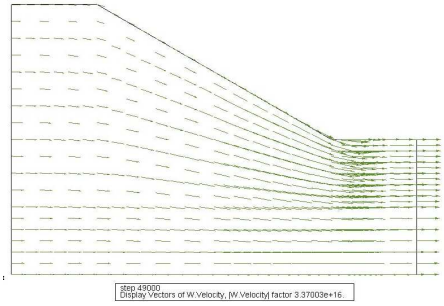

Fig. 4. Water flow vectors at the end of the second run

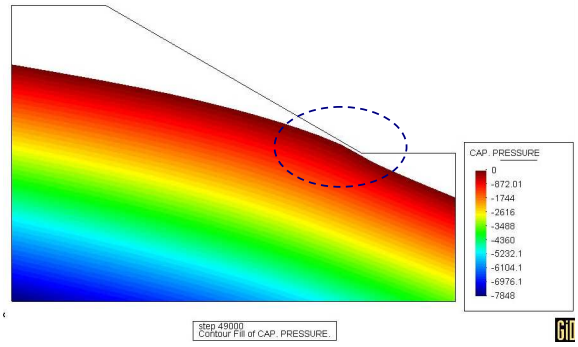

Fig. 5. Free surface at the end of the second run

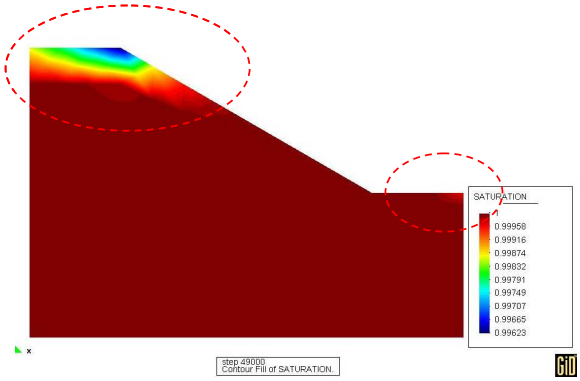

Fig. 6. Water saturation contour at the end of the second run

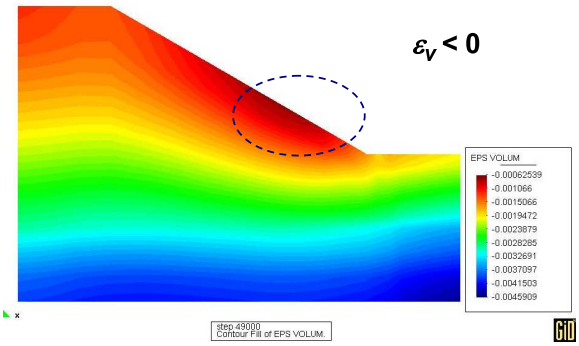

Fig. 7. Volumetric strain contour at the end of the second run

With the third run, the experimental water load of 1.6 kPa was applied at the left third of the bottom surface of the slope.

The case using a dilatant angle of 0^0 is now summarized, as described in detail by Sanavia and Schrefler (2005). The water pressure gradient applied at the lower boundary caused an increase of the level of the free surface up to lower part of the slope, similarly to the case with a dilatant material (see Figure 12). After 91.5 s, the numerical solution became unstable and the numerical convergence was lost; we can assume that the experimentally observed local failure of the slope is described because the plastic strains are concentrated in the lower part of the slope (the equivalent plastic strain contour is very similar to the case with dilatant solid skeleton, Figure 13, and hence is not plotted here; the interested reader is referred to Sanavia and Schrefler 2005). Moreover, the maximum water velocity is concentrated in the lower part of the slope (Figure 11), as experimentally observed.

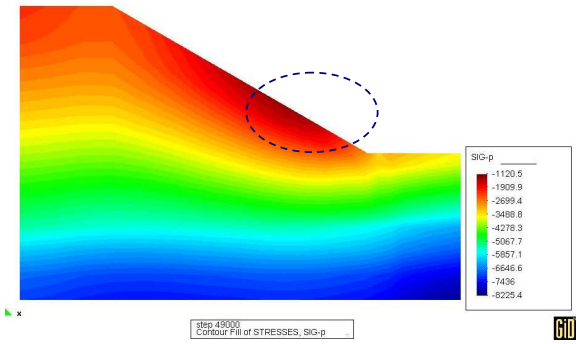

Fig. 8. Mean effective pressure p' contour at the end of the second run

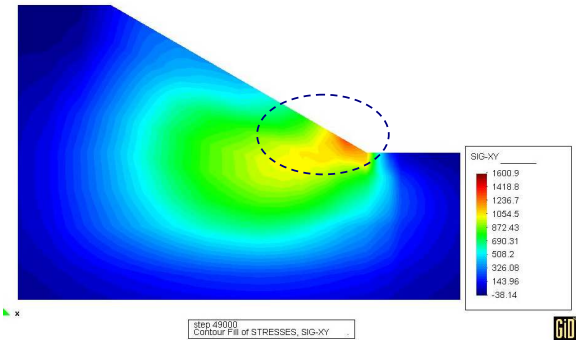

Fig. 9. Shear stress τ'_{xy} contour at the end of the second run

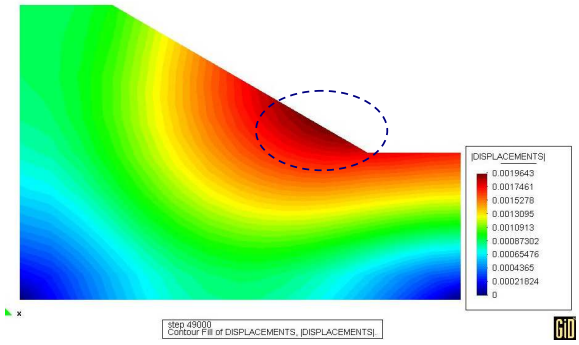

Fig. 10. Displacements contour at the end of the second run

The simulation which assume a slightly dilatant material ($\varphi = 5^0$) is more interesting because it reveals the capability of the multiphase approach to deal with such kind of problems.
Again, the water pressure gradient applied at the lower boundary caused an

increase of the level of the free surface up to the lower part of the slope, as it can be seen in Figure 12. The initiation of the slope failure occurred after 135 s, because the volumetric plastic behaviour of the material increases the stiffness of the solid skeleton, and hence delays the development of the phenomenon. The plastic strains was concentrated in the lower part of the slope (Figure 13), as experimentally observed (Klubertanz, 1999; Klubertanz et al., 2003). At this local failure, the free surface decreased a little (Figure 14) and the maximum water velocity was concentrated in the failure zone (Figure 15), as experimentally observed. Because of the rapid plastic dilatation (see Figure 16, where positive volumetric strain are observed only inside the zone of inelastic strains, and Figure 22), the plastic zone became partially saturated (Figure 17) due to a formation of vapour (Figure 18) and the free surface was pushed down (Figure 14). The displacements are higher in the failure zone, as experimentally observed (Figure 19).

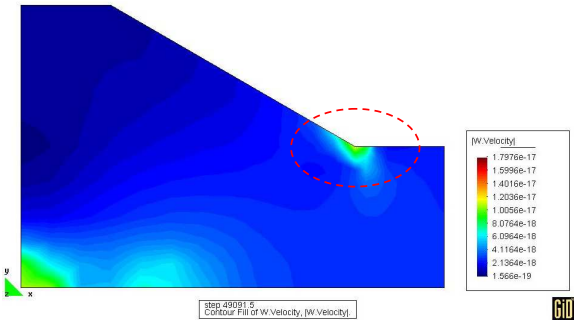

Fig. 11. Water velocity contour at the end of the third run (at 91.5 s), with $\varphi = 0^0$

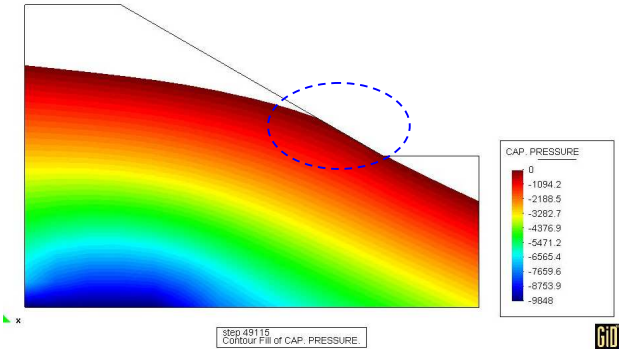

Fig. 12. Capillary pressure contour after 115 s of the third run, with $\varphi = 5^0$

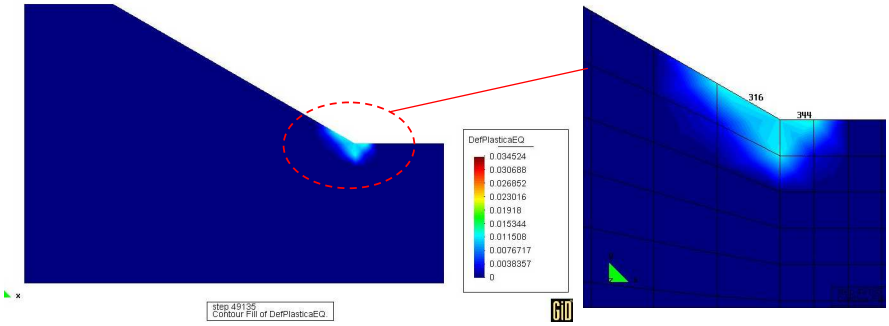

Fig. 13. Equivalent plastic strain contour at the end of the third run (at 135 s), with $\varphi = 5^0$

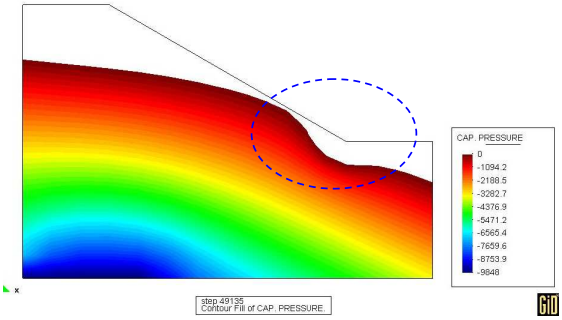

Fig. 14. Capillary pressure contour at the end of the third run (at 135 s), with $\varphi = 5^0$

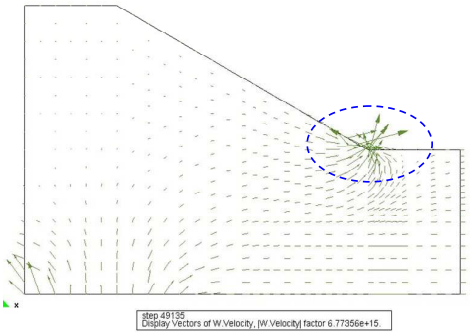

Fig. 15. Water flow vectors at the end of the third run (at 135 s), with $\varphi = 5^0$

A closer look inside the plastic zone reveals that the stress state of the material in its natural state (i.e. at the end of the second run) is closed to the Drucker-Prager yield surface (point A in Figure 20) and reaches the yield

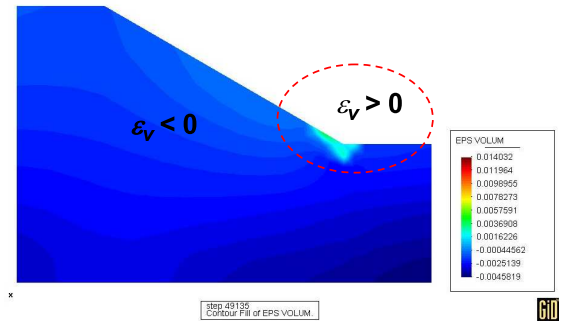

Fig. 16. Volumetric strain contour at the end of the third run (at 135 s), with $\varphi = 5^0$

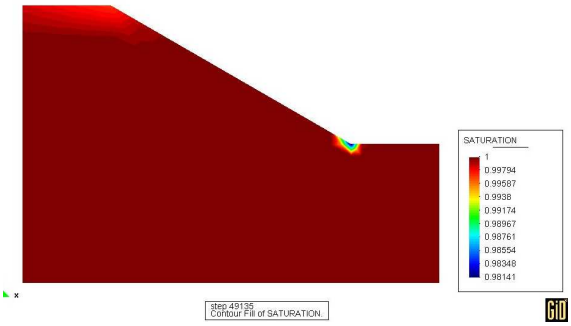

Fig. 17. Water saturation contour at the end of the third run (at 135 s), with $\varphi = 5^0$

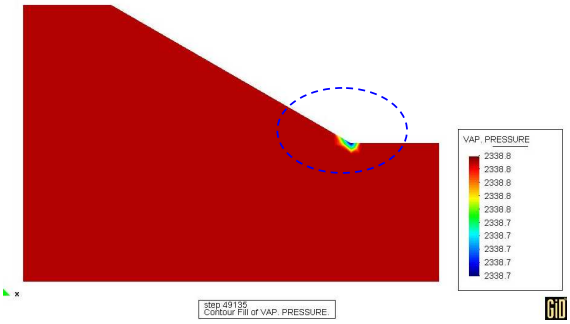

Fig. 18. Vapour pressure contour at the end of the third run (at 135 s), with $\varphi = 5^0$

surface (point B in Figure 20) because of the increase of the water pressure (point B in Figure 21).

Once the stress state is on the yield surface, as a consequence of the increase of water pressure and the softening behaviour of the solid skeleton

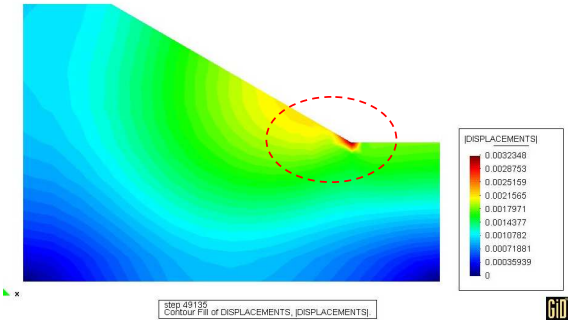

Fig. 19. Displacements contour at the end of the third run (at 135 s), with $\varphi = 5^0$

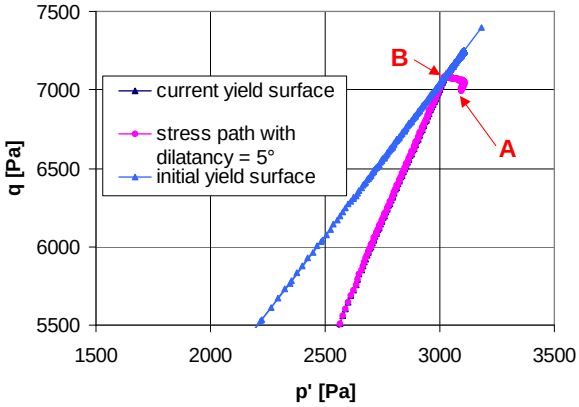

Fig. 20. $p' - q$ stress path during the third run

(see Table 1), the stress state remains on the yield surface (Figure 20) and plastic strains continue to develop (Figure 22) up the failure (at which the cohesion becomes zero because of its softening behaviour, see eq. (8)). When the volumetric strain becomes positive because of the dilatant behaviour of the solid skeleton (Figure 23), the water pressure decreases and becomes negative (Figure 21), reaching in this case the value of the saturation water pressure at ambient temperature with the development of vapour (Figure 18). Temperature and gas pressure at the nodes of the mesh do not change in time, practically, and hence their contours have not been included in this paper.

In case of isochoric material (dilatant angle $\varphi = 0^0$), the local behaviour is quite similar to the case of dilatant material (unlike the volumetric strain behaviour due to its plastic part), as it can be observed in Figures 21, 22 and 23.

Moreover, additional aspects can be noted in the time histories just explained, as for example the influence of dilatancy on the water pressure evolution. In fact, in Figures 21, 22 and 23, it can be observed that smaller p^w

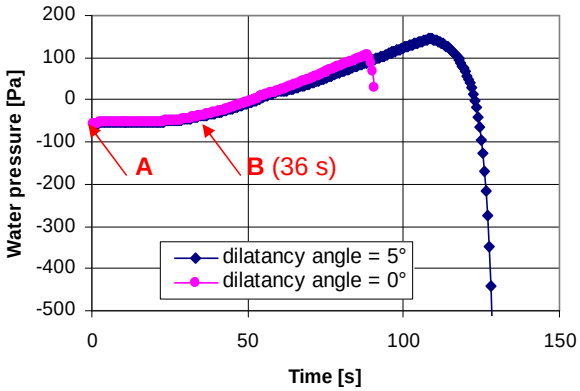

Fig. 21. Water pressure history during the third run

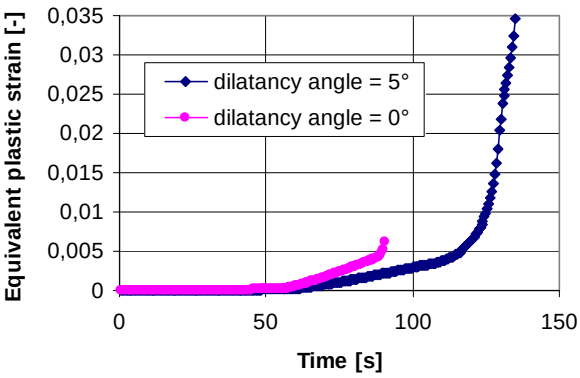

Fig. 22. Equivalent plastic strain history during the third run

develops in case of dilatant material since the early times. This influence increases with the development of plastic strains and strongly affects the water pressure evolution when the plastic strain rate becomes high.

The numerical example has been solved also for $\varphi = 10^0$ and $\varphi = 20^0$. The numerical results are qualitatively similar to those obtained with $\varphi = 5^0$ and hence are not written here. However, they are of some interest because they show how the time of the initiation of slope failure decreases with the dilatant angle, as it is summarized in Table 2. This is a noteworthy result because it has been observed experimentally (e.g. Tika and Hutchinson, 1999) and is one of the reason that contributes to explain the very fast collapse of the Vajont catastrophic landslide (Hendron and Patton, 1985), which occurred in Italy on October 9, 1963 (a slide of 270 million m^3 of rock moved in $20-25$ s, with a velocity of $20-30$ m/s; 2043 persons died and 8 villages were destroyed).

Finally, the comparison between the measured and computed displacements contour, Figure 24 and Figure 19, respectively, reveals that the value

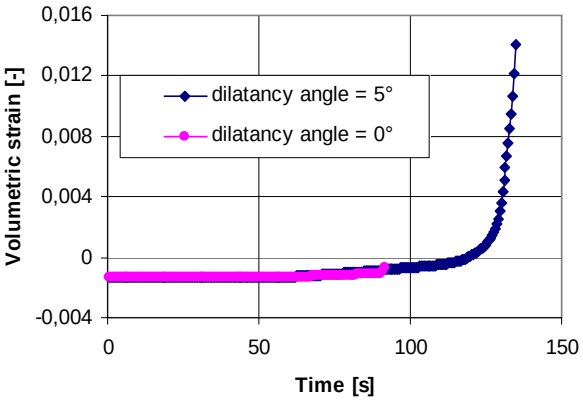

Fig. 23. Volumetric strain history during the third run

Table 2. Influence of the dilatant angle on the time of the slope failure initiation

Dilatancy	Failure time
20^0	235 s
10^0	175 s
5^0	135 s
0^0	91.5 s

of the maximum displacement is captured, while the general shape is different. This is probably due to a limit of the used Drucker-Prager model, which assumes homogeneous elastic parameters. The comparison between the measured and computed water pressure in some points, Figure 25 for the case with dilatant material, shows a quite good agreement (the location of those points is indicated in the caption of Figure 25).

The aspects of the regularization properties of the multiphase model when the solid skeleton obeys to a softening behaviour are beyond the aim of this paper. The interested reader can see, e.g., Zhang et al. (1999), Ehlers and Volk (1999) and Zhang et al. (2007) for some recent findings.

5 Conclusions

In this work, a finite element analysis of the initiation of a slope failure in a small-scale laboratory test has been analyzed by using a non-isothermal elasto-plastic multiphase model. To this end, the mathematical formulation for the hydro-thermo-mechanical behaviour of water saturated and partially saturated porous materials has been summarized. The numerical results of a slope failure experimental test loaded by a pore pressure boundary condition have been presented. It has been shown that the multiphase modelling is able

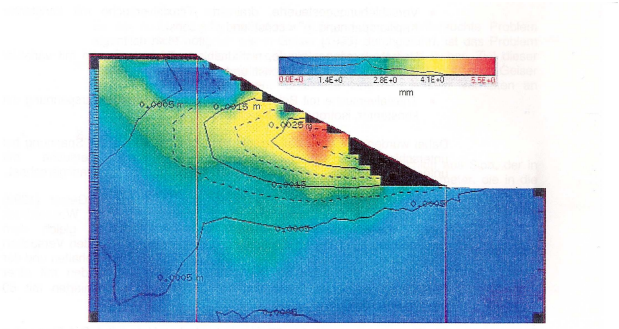

Fig. 24. Experimental displacements contour (Klubertanz, 1999)

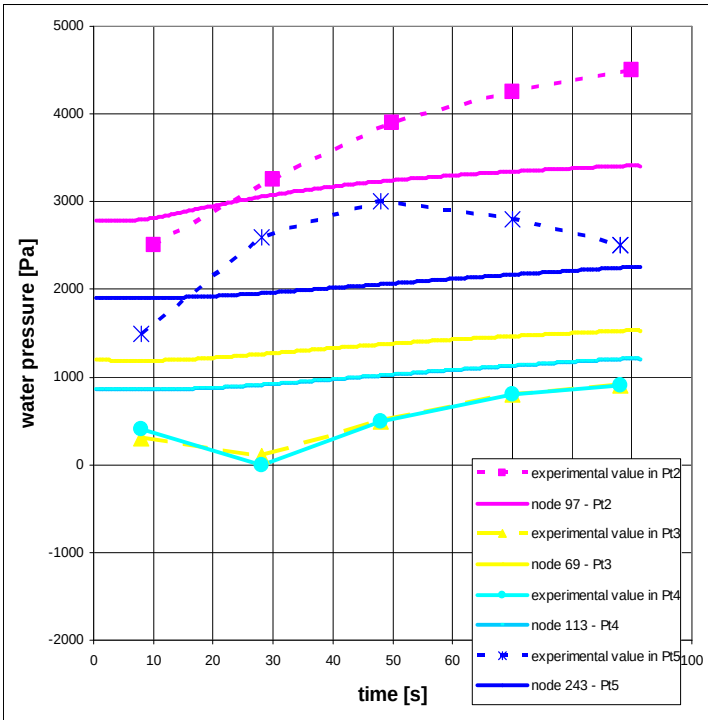

Fig. 25. Comparison between experimental and numerical water pressures in the points with coordinates: Pt2 (0.40, 0.40), Pt3 (0.40, 0.60), Pt4 (0.60, 0.60), Pt5 (0.90, 0.40)

to capture the main experimental observations at global level such as the local failure zone at the onset of slope failure and the outflow appeared in that zone. This modelling approach, by the analysis of the THM computations at local

level, also permits to understand the triggering mechanisms of the failure zone.

In addition, the development of a vapour phase within the dilatant plastic zone points out that with a sufficiently general THM model different situations can be modelled. This aspect justifies the use of a non-isothermal formulation for the appropriate analysis of the water phase change from a physical point of view. Moreover, the non-isothermal approach could be useful for the analysis of the onset of shallow landslides in partially saturated slopes, where the exchange of relative humidity with the atmosphere could play a role.

In the author experience, it can be concluded that the multiphysics approach looks very promising for the analysis of the onset of landslides, provided that the constitutive models for the multiphase porous media in saturated/unsaturated conditions and the related mechanical and hydraulic properties are described with sufficient accuracy.

Acknowledgements

This research was developed within the framework of *Lagrange Laboratory*, a European research group between CNRS, CNR, University of Rome Tor Vergata, University of Montpellier II, ENPC and LCPC. The author would like to acknowledge the University of Padua (*UNIPD CPDA*034312) for the financial support, Prof. Lyesse Laloui (EPFL, Lausanne, CH) and Dr. George Klubertanz (Emch+Berger AG, Bern, CH) for helpful discussions. Appreciation is also extended to Eng. Matteo Foffani (Padua, I) for his co-operation in the computations.

Bibliography

Alonso, E.E., Gens, A. and Josa, A. (1990), "A constitutive model for partially saturated soils", *Géotechnique*, Vol. 40, pp. 403–430.

Bertrand, F. and Laloui L. (2008), "ACMEG-TS: a constitutive model for unsaturated soils under non-isothermal conditions", *Int. J. Numer. Anal. Meth. Geomech.*, doi:10.1002/nag.712.

Bolzon, G., Schrefler, B.A. and Zienkiewicz O.C. (1996), "Elastoplastic soil constitutive laws generalized to partially saturated states", *Géotechnique*, Vol. 46, pp. 279–289.

Bolton, M.D., Take, W.A., Wong, P.C.P. and Yeung F.J. (2003), "Mechanisms of failure in fill slopes after intense rainfall", Keynote Paper, Int. Conf. on Slope Engineering, Hong Kong, China, pp.125.

Borja, R.J. (2004), "Cam-clay plasticity. Part V: A mathematical framework for three-phase deformation and strain localisation analyses of partially saturated porous media", *Comp. Methods Appl. Mech. Engrg.*, Vol. 193, pp. 5301–5338.

Cascini, L., Sorbino, G. and Cuomo S. (2005), "Flow-like mass movements in pyroclastic soils: remarks on the modeling of triggering mechanisms", *Rivista Italiana di Geotecnica*, Vol. 4, pp. 11–31.

Dikau, R., Brundsen, D., Schrott, L. and Ibses M.L. (1996), *Landslide Recognition*, John Wiley & Sons.

Ehlers, W. and Volk, W., (1999), "Localization Phenomena in Liquid-Saturated and Empty Porous Solids", *Transport in Porous Media*, Vol. 34, pp. 159–177.

Ehlers, W., Graf, T. and Ammann M. (2004), "Deformation and localization analysis in partially saturated soil", *Comp. Methods Appl. Mech. Engrg.*, Vol. 193, pp. 2885–2910.

Fernandez Merodo, J.A., Pastor, M.,Mira, P., Tonni L., Herreros, M.I., Gonzalez E. and Tamagnini R. (2004) "Modelling of diffuse failure mechanisms of catastrophic landslides", *Comp. Methods Appl. Mech. Engrg.*, Vol. 193, pp.2911–2939.

Gawin, D., Baggio, P. and Schrefler B.A. (1995), "Coupled heat, water and gas flow in deformable porous media", *Int. J. Num. methods in Fluids*, Vol. 20 No.7, pp. 967–987.

Gray, W.G. and Hassanizadeh, M. (1991), "Unsaturated Flow Theory including Interfacial Phenomena", *Water Resources Res.*, Vol. 27 No.8, pp. 1855–1863.

Gray, W.G. and Schrefler, B.A. (2001), "Thermodynamic approach to effective stress in partially saturated porous media", *Eur. J. Mech. A/Solids*, Vol. 20, pp. 521–538.

Hassanizadeh, M. and Gray, W.G. (1979a), "General Conservation Equations for Multi-phase System: 1. Averaging technique", *Adv. Water Res*, Vol. 2, pp. 131–144.

Hassanizadeh, M. and Gray, W.G. (1979b), "General Conservation Equations for Multi-Phase System: 2. Mass, Momenta, Energy and Entropy Equations", *Adv. Water Res*, Vol. 2, pp. 191–201.

Hassanizadeh, M. and Gray, W.G. (1980), "General Conservation Equations for Multi-Phase System: 3. Constitutive Theory for Porous Media Flow", *Adv. Water Res*, Vol. 3, pp. 25–40.

Hendron, A.J. and Patton, F.D. (1985), *The Vaiont slide, a geotechnical analysis based on new geologic observations of the failure surface*, Technical Report GL-85-5. Washington DC, Department of the Army US Corps of Engineers vol. I.

Klubertanz G. (1999), *Zur hydromechanischen Kopplung in dreiphasigen porsen Medien*, Ph.D. Thesis n.2027, Lausanne: Ecole Polytechnique Fdrale de Lausanne.

Klubertanz, G., Bouchelaghem, F., Laloui, L. and Vulliet L. (2003), "Miscible and immiscible multiphase flow in deformable porous media", *Mathematical and Computer Modelling*, Vol. 37, pp. 571–582.

Lewis, R.W. and Schrefler B.A. (1987), *The Finite Element Method in the Deformation and Consolidation of Porous Media* (1st edn). Wiley & Sons, Chichester.

Lewis, R.W. and Schrefler B.A. (1998), *The Finite Element Method in the Static and Dynamic Deformation and Consolidation of Porous Media*, John Wiley & Sons, Chichester, UK.

Nuth, M. and Laloui, L. (2008), "Effective stress concept in unsaturated soils: Clarification and validation of a unified approach", *Int. J. Numer. Anal. Meth. Geomech.*, doi:10.1002/nag.645.

Pastor, M., Fernandez Merodo, J.A., Gonzalez, E., Mira, P., Li, T. and Liu X. (2004a), "Modelling of Landslides: (I) Failure Mechanisms, in: Darve F. and Vardoulakis I. (Ed.) *Degradations and Instabilities in Geomaterials*, CISM Courses and Lectures No. 461, Springer-Verlag.

Pastor, M., Quecedo, M., Gonzalez, E., Herreros, M.I., Fernandez Merodo, J.A. and Mira P. (2004b), "Modelling of Landslides: (II) Propagation", in: Darve F. and Vardoulakis I. (Ed.), *Degradations and Instabilities in Geomaterials*, CISM Courses and Lectures No. 461, Springer-Verlag.

Pastor, M., Quecedo, M., Gonzalez, E., Herreros, M.I., Fernandez Merodo, J.A. and Mira P. (2004c), "Numerical modelling of the propagation of fast landslides using the finite element method", *Int. J. Numer. Meth. Engrg*, Vol. 59, pp. 755–794.

Sanavia, L. and Schrefler, B.A. (2005), "Finite element analysis of the initiation of landslides with a multiphase model", *Proceedings, 3rd Biot Conference on Poromechanics*, Abousleiman, Y., Cheng, A.H.-D., and Ulm, F.-J. (Ed.), Poromechanics III-Biot Centennial (1905-2005), A.A. Balkema, Leidon/London/New York/Philadelphia/Singapore, pp. 397–402.

Sanavia, L., Schrefler, B.A. and Steinmann, P. (2002), "A formulation for an unsaturated porous medium undergoing large inelastic strains", *Computational Mechanics*, Vol. 28, pp. 137–151.

Sanavia, L., Pesavento, F. and Schrefler B.A. (2006), "Finite element analysis of non-isothermal multiphase geomaterials with application to strain localisation simulation", *Computational Mechanics*, Vol. 37, pp. 331–348.

Schrefler, B.A. (1984), *The Finite Element Method in Soil Consolidation (with applications to Surface Subsidence)*, Ph.D. Thesis, University College of Swansea, C/Ph/76/84, Swansea, UK.

Schrefler, B.A. (2002), "Mechanics and Thermodynamics of Saturated-Unsaturated Porous Materials and Quantitative Solutions", *Applied Mechanics Review*, Vol. 55 No.4, pp. 351–388.

Schrefler, B.A., Simoni, L., Li, X. and Zienkiewicz, O.C. (1990), "Mechanics of partially saturated porous media", in Desai C.S. and Gioda G. (Ed.), *Numerical Methods and Constitutive Modelling in Geomechanics*, CISM Courses and Lectures No 311, Springer-Verlag, pp. 169–209.

Tacher, L., Bonnard, C., Laloui, L. and Parriaux A. (2005), "Modelling the behaviour of a large landslide with respect to hydrogeological and geomechanical parameter hererogeneity", *Landslides*, Vol. 2, pp. 3–14.

Tika, T.E. and Hutchinson, J.N. (1999), "Ring shear testes on soil from the Vaiont landslide slip surface", *Géotechnique*, Vol. 49 No.1, pp.59–74.

Zhang, H.W., Sanavia, L. and Schrefler, B.A. (1999), "An internal length scale in dynamic strain localisation of multiphase porous media", *Mechanics of Cohesive-Frictional Materials*, Vol. 4, pp. 443–460.

Zhang, H.W., Sanavia, L. and Schrefler B.A. (2000), "Numerical analysis of dynamic strain localisation in initially water saturated dense sand with a modified generalised plasticity model", *Computers and Structures*, Vol. 79, pp. 441–459.

Zhang, H.W., Qin, J.M., Sanavia, L. and Schrefler B.A. (2007), "Some theoretical aspects of strain localization analysis of multiphase porous media with regularized constitutive models", *Mechanics of Advanced Materials and Structures*, Vol. 14 No.2, pp. 107–130.

Zienkiewicz, O.C., Chan, A., Pastor, M., Schrefler, B.A. and Shiomi T. (1999), *Computational Geomechanics with special Reference to Earthquake Engineering*, John Wiley & Sons, Chichester.